

ARTICLE

Open Access

Optical actuation of a micromechanical photodiode via the photovoltaic-piezoelectric effect

A. Rampal^{1,2} and R. N. Kleiman¹ 

Abstract

Radiation pressure and photothermal forces have been previously used to optically actuate micro/nanomechanical structures fabricated from semiconductor piezoelectric materials such as gallium arsenide (GaAs). In these materials, coupling of the photovoltaic and piezoelectric properties has not been fully explored and leads to a new type of optical actuation that we call the photovoltaic-piezoelectric effect (PVPZ). We demonstrate this effect by electrically measuring, via the direct piezoelectric effect, the optically induced strain in a novel torsional resonator. The micron-scale torsional resonator is fabricated from a lattice-matched single-crystal molecular beam epitaxy (MBE)-grown GaAs photodiode heterostructure. We find that the strain depends on the product of the electro-optic responsivity and piezoelectric constant of GaAs. The photovoltaic-piezoelectric effect has important potential applications, such as in the development of configurable optical circuits, which can be used in neuromorphic photonic chips, processing of big data with deep learning and the development of quantum circuits.

Introduction

Optical actuation of micro/nanomechanical resonators has been developed across various material platforms and geometries^{1–23}. Of particular interest is optical actuation of semiconductor materials^{1–15}, given their technological ubiquity in devices such as computers, cell phones, solar cells, lasers, photodiodes, and micro/nanomechanical sensors. One of the main reasons for their ubiquity stems from the capability for high-volume, high-yield manufacturing of micro/nanodevices.

The most common mechanisms used for optical actuation are radiation pressure and photothermal forces. Radiation pressure is a weak force; hence, large optical intensities and/or complex optical setups are required, which limits the circumstances in which these forces can be used. Mechanical structures actuated photothermally can undergo large strains, but their frequency response is

limited by the thermal constants of the materials. A further limitation of these mechanisms is that extra steps are required to integrate an electrical transducer to quantify the optically induced strain. The extra steps can come either in the form of additional fabrication steps for integration of a transducer^{11,14,15} or via complicated experimental setups to integrate a transducer external to the device^{3,5,7–10,12}. These constraints limit the use of optical actuation to either lab settings or customized applications in commercial settings.

Here, we introduce and demonstrate a new optical actuation mechanism that we call the photovoltaic-piezoelectric (PVPZ) effect. This effect can occur in semiconductor materials that possess both piezoelectric and photovoltaic properties such as those in the III–V and II–VI compound semiconductor families. The piezoelectric property enables coupling between the mechanical and electrical degrees of freedom (DOFs) via the inverse and direct piezoelectric effects. In these effects, an applied voltage results in a mechanical strain, and a mechanical strain results in a charge, respectively. Using

Correspondence: A. Rampal (abhi.rampal@gmail.com)

¹Department of Engineering Physics, McMaster University, Hamilton, ON L8S 4L7, Canada. ²Present address: CircuitMind Inc, 185 Spadina Avenue, Toronto, ON M5T 2C6, Canada

© The Author(s) 2021



Open Access This article is licensed under a Creative Commons Attribution 4.0 International License, which permits use, sharing, adaptation, distribution and reproduction in any medium or format, as long as you give appropriate credit to the original author(s) and the source, provide a link to the Creative Commons license, and indicate if changes were made. The images or other third party material in this article are included in the article's Creative Commons license, unless indicated otherwise in a credit line to the material. If material is not included in the article's Creative Commons license and your intended use is not permitted by statutory regulation or exceeds the permitted use, you will need to obtain permission directly from the copyright holder. To view a copy of this license, visit <http://creativecommons.org/licenses/by/4.0/>.

both effects together, mechanical strain can not only be electrically induced but also measured. Both of these effects are utilized in research and commercial piezoelectric pressure sensors^{24,25} and accelerometers^{26,27} to measure the strain resulting from external forces. Similarly, resonant quartz tuning forks making use of both the inverse and direct piezoelectric effects are employed in scanning probe microscopy^{28,29} and atomic force microscopy^{30,31} for imaging topographical features of material surfaces. Building on the photovoltaic effect and the inverse piezoelectric effect, the optical actuation is a result of a two-step process in which the incident light induces a photovoltage that causes mechanical strain. Making use of the direct piezoelectric effect, the mechanical strain can be electrically measured directly, hence mitigating the need for extra fabrication steps or complicated experimental setups for the integration of a transducer. The PVPZ effect therefore couples the optical, electrical, and mechanical DOFs of the material. Broadly speaking, the PVPZ effect leads to relatively large forces with a geometry-limited frequency response.

We demonstrate the PVPZ effect using a single-crystal micromechanical device fabricated from a GaAs p-n junction photodiode-solar cell heterostructure, with heterostructure layers added to ensure successful release of the mechanical resonator. GaAs is chosen because it is commonly used to make high-efficiency photodiode-based solar cell structures^{32–35} and has a robust piezoelectric effect^{36–38}. Piezoelectric micromechanical devices fabricated from GaAs heterostructures have previously been studied. For example, Masmanidis et al.³⁶ demonstrated electrical tuning of the device resonant frequency in a GaAs PIN structure. In their studies, the device was electrically driven, and its mechanical strain was measured using optical interferometry. Okamoto et al.³⁹ demonstrated dynamic mechanical coupling between two GaAs bridge structures. In their studies, the devices were electrically driven using the inverse piezoelectric effect, and their motion was detected using the direct piezoelectric effect, as in quartz tuning fork resonators. Our micromechanical structure is a novel planar torsional resonator designed to minimize clamping losses and null out residual photothermal actuation. We chose to use the direct piezoelectric effect to provide a direct measure of deflection due to the seamless and natural integration with the device structure. We also use the indirect piezoelectric effect for electrical actuation of the device for calibration purposes. Our device has a resonant frequency of 76.7 kHz, a room-temperature Q of ~ 6000 and an electro-optic responsivity of 0.178 A/W. We find that the optically induced strain resulting from the PVPZ effect depends on the product of the electro-optic responsivity and the piezoelectric constant and that this strain is linear with optical power, with a nonresonant tip deflection of $\delta_z \sim 11 \mu\text{m/W}$.

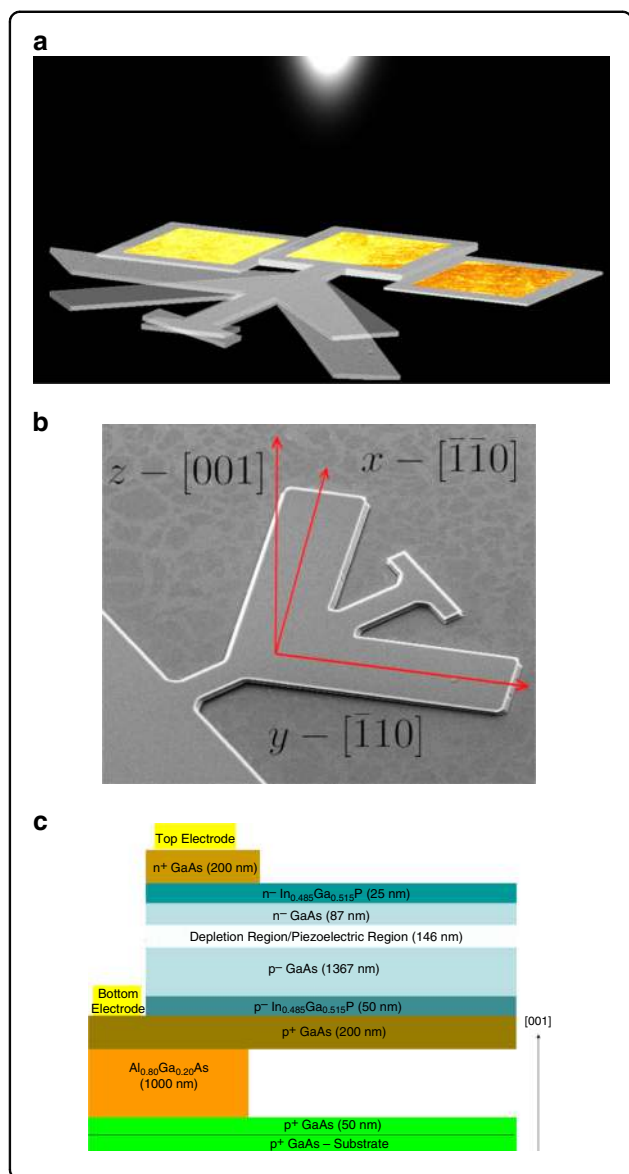
The demonstration of the PVPZ effect extends the application of semiconductors to the optoelectromechanical domain, addressing the long-standing open issue of providing optical actuation in a semiconductor platform for all-optical computing, processing, and telecommunication applications. The advantages of using semiconductor materials are the ability to make use of conventional batch fabrication methods and the opportunity to leverage mature highly integrated on-chip optical and electronic functionalities.

Results and discussion

We experimentally demonstrate the PVPZ effect by optically actuating a novel micromechanical structure, a planar torsional resonator (Fig. 1a), and electrically measuring the resulting optically induced strain near resonance via the direct piezoelectric effect. The torsional resonator is fabricated from an epitaxially grown GaAs photodiode heterostructure (Supplementary Section I). The torsional deformation arises from the antisymmetric flexural bending of the two diagonally oriented tines that comprise the structure. The driving force for this antisymmetric bending is the result of (a) using the antisymmetric piezoelectric property of GaAs in the plane of the device and (b) designing the photodiode heterostructure with vertical asymmetry about the neutral plane to resemble a unimorph structure. The former can be understood by considering the piezoelectric matrix for a [001]-oriented wafer of GaAs, a III–V semiconductor having a zincblende crystal structure³⁷:

$$d_{ij} = \frac{d_{14}}{2} \begin{bmatrix} 0 & 0 & -\beta \\ 0 & 0 & \beta \\ 0 & 0 & 0 \\ 2\alpha & 2\beta & 0 \\ -2\beta & 2\alpha & 0 \\ 0 & 0 & 0 \end{bmatrix} \quad (1)$$

where d_{ij} are the piezoelectric coefficients, $\beta = \cos(2\phi)$, $\alpha = \sin(2\phi)$ and ϕ is the rotation angle about the [001]-direction with respect to the $[\bar{1}\bar{1}0]$ -direction, $\phi = 0$. For GaAs, $d_{14} = 1.345 \text{ pm/V}$. To make use of the planar antisymmetry, the two tines of the torsional resonator are aligned parallel to the two orthogonally oriented [110]-directions (Fig. 1b). According to this matrix, d_{13} and d_{23} are equal in magnitude but opposite in sign; hence, an electric field applied in the [001]-direction results in equal but opposite longitudinal strains, ϵ , in the $[\bar{1}\bar{1}0]$ - and $[\bar{1}10]$ -directions, where $\epsilon_1 = d_{13}E_3$ and $\epsilon_2 = d_{23}E_3$, respectively. The flexural bending of the tines, required for driving and detecting, is achieved by designing the GaAs heterostructure such



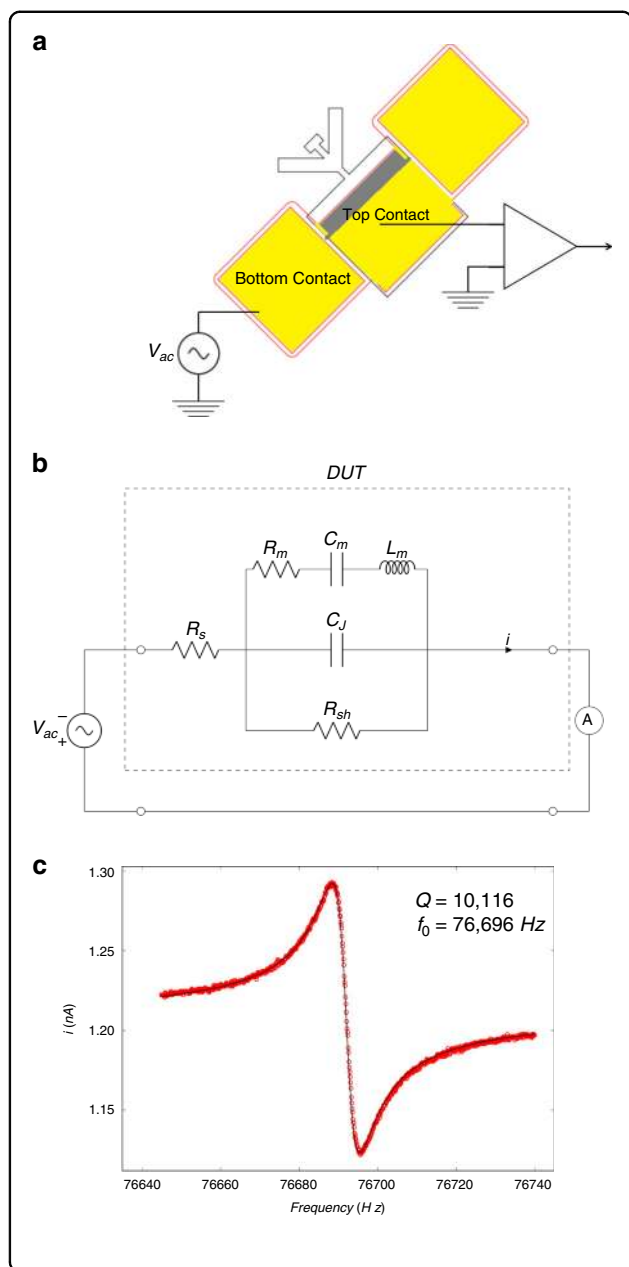
that the piezoelectric layer is offset from the neutral surface of the tines, in this case near the upper surface of the device (Fig. 1c). The depletion region of the p-n junction of the GaAs photodiode responds similarly to a dielectric material, so an applied voltage leads to a piezoelectric stress. The n- and p-type layers are sufficiently doped to serve as equipotential surfaces for device actuation without the need for metal contact layers that would be opaque to optical illumination. The heterostructure is grown by molecular beam epitaxy (MBE) on a p^+ GaAs substrate and consists of a 1.0- μm -thick $\text{Al}_{0.8}\text{Ga}_{0.2}\text{As}$ sacrificial etch layer followed by a 2.075- μm -thick photodiode structure resembling a GaAs solar cell. The doping concentrations and thicknesses of the individual layers (Supplementary Section III) are

Fig. 1 Design of the photodiode torsional resonator.

a Fundamental undeformed torsional mode shape (semitransparent) and deformed mode shape of the resonator under optical illumination. The illustrated mode shape is determined from simulations (as shown in Supplementary Section V). The resonator is composed of a central spine terminated on the top by a rectangular pad and at the bottom by an anchor, where three contact pads are situated. Protruding from the spine at $\pm 45^\circ$ are two tines. The electrodes on the anchor facilitate measurement of the piezoelectric current. Above-bandgap light is modulated near the resonant frequency of the resonator, exciting the torsional mode via the PVPZ effect. **b** SEM image of a fabricated torsional resonator on a [001] GaAs wafer. The spine is parallel to the [100]-direction (not marked). The directions of the tines are chosen to exploit the antisymmetry in the III-V piezoelectric properties, resulting in antisymmetric flexural deformation. **c** Cross-section (not to scale) of the MBE-grown photodiode heterostructure. The section shown is the released structure, i.e., the $\text{Al}_{0.8}\text{Ga}_{0.2}\text{As}$ layer remains in place at the anchor and is removed below the spine and tines. The depletion region is intentionally placed above the neutral plane to enable unimorph-type actuation. The arrow indicates the crystal orientation. The top and bottom electrodes contacting the n^+ and p^+ GaAs layers are used to measure the piezoelectric current resulting from the induced strain. The electrodes can also be used to electrically drive the resonator. The center contact pad shown in Fig. 1a connects to the device top electrode, while the two adjacent contact pads connect to the device bottom electrode

chosen to achieve successful fabrication of the torsional resonator⁴⁰ and to maximize both the photocurrent and piezoelectric current. The torsional resonator design is chosen to null out, to a first approximation, the driving force from photothermal effects because uniform illumination would result in symmetric photothermal bending of the tines. The PVPZ effect is not unique to this geometry and could be demonstrated and utilized in simpler cantilever structures since the use of both d_{13} and d_{23} is not required.

In the first set of measurements, we actuate the resonator structure electrically by making use of the inverse piezoelectric effect and measure its motion using the current from the direct piezoelectric effect, providing direct characterization of the device and its piezoelectric and mechanical properties. This permits us to determine the electromechanical device properties entirely in the electric domain using traditional analysis methods⁴¹. The electromechanical transduction is characterized by applying an AC voltage at frequencies near the resonant frequency (Fig. 2a) across the device and fitting the measured electrical response to the modified Butterworth-van Dyke (BVD) model (Fig. 2b). The measured response (Fig. 2c) agrees very well with the modified BVD model. Using the definitions $\omega_0^2 = 1/(L_m C_m)$ and $Q = 1/(\omega_0 R_m C_m)$, the resonator is found to have a Q of 10,116 and a resonant frequency of $f_0 = \omega_0/2\pi = 76,696$ Hz, which are consistent with expectations from finite element simulations⁴⁰. The resonator dimensions for the



tine, spine, and pad are $80 \times 30 \mu\text{m}$, $102.5 \times 10 \mu\text{m}$, and $40 \times 15 \mu\text{m}$, respectively, with a total released device thickness of $1.875 \mu\text{m}$. All measurements are performed at room temperature. The high value of Q at room temperature is expected because the resonator is designed such that the torsional mode has minimal clamping losses resulting from it being supported at the nodal point^{42,43}. The motional capacitance C_m can be analytically related to the mechanical mode, device geometry, and piezoelectric coefficient (Supplementary Section VII). The junction capacitance, C_J , is dominated by the contact pad, which is much larger in area than the device itself. As a result, the background (or feedthrough) current from C_J is

Fig. 2 Electrical actuation of the photodiode torsional resonator.

a Experimental setup for electrically inducing piezoelectric strain and measuring piezoelectric charge. A function generator, represented as V_{ac} , supplies the AC signal required to drive the resonator near its resonant frequency. The piezoelectric current is first preamplified and then measured using an SR844 Lock-In Amplifier. The resonator and the preamplifier are placed in a vacuum chamber at a pressure of ~ 2 mTorr. **b** Equivalent circuit of the modified BVD model of a piezoelectric resonator arranged for standard two-terminal drive and detection. The motional components, R_m , C_m and L_m , are the electrical analogs of a damped harmonic oscillator representing the mechanical dissipation, spring constant, and mass of the resonator, respectively. C_J is the junction capacitance or geometric capacitance of the device, R_{sh} is primarily due to the shunt resistance of the diode, R_s is dominated by the series resistance of the metal-semiconductor contacts, and i is the piezoelectric current. The dashed line encompasses the equivalent circuit of the resonator or device under test (DUT). **c** Frequency response of the measured RMS current with a drive voltage of $66 \mu\text{V}_{\text{rms}}$. The solid line is a fit to the data using equation (S4) derived for the circuit shown in Fig. 2b, and the fitted parameters are given in Supplementary Section VIII. The resonator dimensions for the tine, spine, and pad are $80 \times 30 \mu\text{m}$, $102.5 \times 10 \mu\text{m}$, and $40 \times 15 \mu\text{m}$, respectively, with a total released device thickness of $1.875 \mu\text{m}$

large, which leads to a large offset in the current, as shown in Fig. 2c.

In a second set of measurements, we calibrate the optical response of the photodiode using a DC voltage source and an infrared LED (Fig. 3a) with a peak wavelength of 830 nm and a photon energy just higher than the bandgap of GaAs. The electro-optic responsivity, R_{resp} , and efficiency of the photodiode in converting optical to electrical power are determined by fitting the measured photocurrent, I , to the single-diode DC photovoltaic (PV) model⁴⁴ shown in Fig. 3b and described by Eq. (S8). The measured photodiode I–V characteristics (Fig. 3c) agree well with this model, and the photodiode is found to have $R_{\text{resp}} = 0.178 \text{ A/W}$ with an efficiency of approximately 11.5%. The responsivity is calculated as the ratio of the short-circuit current, I_{sc} , to the incident optical power, P_{opt} . The short-circuit current is the current measured at $V_{\text{DC}} = 0$, which is closely equivalent to the incident photocurrent, I_{ph} . The efficiency of the photodiode is calculated as the ratio of electrical power at the maximum power point (The maximum power point is defined as a point on the curves in Fig. 3b at which the product of the photocurrent and photovoltage is a maximum) to the incident optical power. In the optical experiments, the LED is placed $\sim 0.5 \text{ cm}$ from the device such that the device is homogeneously illuminated. Experimental details on the measured optical powers are given in Supplementary Section XI.

In a third set of measurements, we actuate the resonator structure optically by making use of the photovoltaic effect in conjunction with the piezoelectric effect and measure its motion using the current from the direct

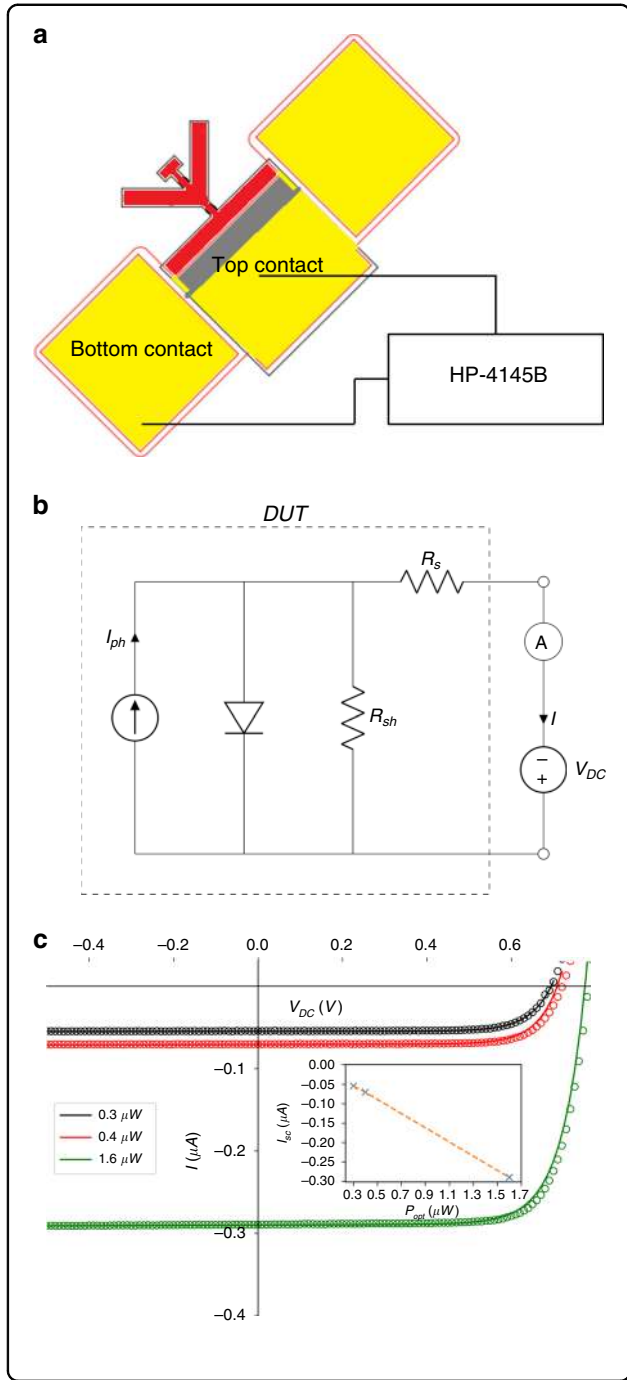


Fig. 3 DC optical responsivity of the photodiode. **a** Experimental setup for measuring I–V curves. The photodiode is illuminated by a DigiKey model TSGH510-ND infrared LED, and an HP-4145B semiconductor parameter analyzer measures the generated photocurrent and applies a DC voltage. The illuminated section of the photodiode is shown in red and illustrates homogeneous illumination. Unlike the resonance measurements, the I–V curves are measured at ambient pressure. **b** Equivalent circuit of the single-diode DC PV model. The photocurrent, I_{ph} , from the photodiode is measured at the output terminals as a function of an externally applied DC voltage, V_{DC} , where I_{ph} is the incident photocurrent. The dashed line encompasses the equivalent circuit of the photodiode or DUT. **c** I–V curves of the illuminated photodiode. The solid lines are a fit to the data using equation (S8) derived from the circuit shown in Fig. 3b, and the fitted parameters are given in Supplementary Section IX. The expected linearity of the short-circuit current I_{sc} with the incident optical power is shown in the inset

or 3b. The equivalent circuit including the actuation and measurement components is shown in Fig. 4b. We set up a parallel RC load branch at the output terminals of the optically driven resonator and measure the current i_L through C_L . The optically driven resonator circuit is highly nonlinear due to the diode properties, with a general expression for i_L given in Rampal⁴⁰ for different load conditions. The expression is strongly dependent on the DC bias point, which in this case is determined primarily by R_L . When $R_L < V_{oc}/I_{sc}$, the device is in the current-dominated regime of the photodiode⁴⁰, where changes in photocurrent, i_1 , are directly related to changes in optical power, as in the DC case, i.e., $i_1 = R_{resp}p_{opt}$ and $I_{ph} = R_{resp}P_{opt}$ for the respective AC and DC cases. The value of R_L must also be chosen so that its impedance is larger than the impedance near resonance of the capacitive components, $C_T = C_J + C_L$, i.e., $\omega R_L C_T > 1$, to maintain a sufficiently high bandwidth to detect the resonant device operation. Based on these considerations, R_L and I_{sc} should be chosen such that $1/(\omega_0 C_T) < R_L < V_{oc}/I_{sc}$, or $11 \text{ k}\Omega < R_L < 11 \text{ M}\Omega$ for our device, and we use a value of $R_L = 1.0 \text{ M}\Omega$ for our measurements. Under these circumstances, we can derive an expression for the complex current, i_L , through the load capacitor – a measurable quantity – by analysis of the equivalent circuit in Fig. 4c:

$$i_L(\omega) = i_1 j \omega C_L Z_t \tag{2}$$

$$|i_L(\omega)| = i_1 \frac{(a - 1) \sqrt{Q^2(\omega_0^2 - \omega^2)^2 + (\omega\omega_0)^2}}{\sqrt{Q^2\left(\omega_0^2 \frac{C_m}{C_j} + a(\omega_0^2 - \omega^2)\right)^2 + (a\omega\omega_0)^2}} \tag{3}$$

where Z_t is the total impedance in parallel with the photodiode, as indicated by the dashed lines in Fig. 4a, and $a \equiv 1 + C_L/C_J$. Circuit analysis shows that the swing

piezoelectric effect. To illustrate the PVPZ effect and hence demonstrate the coupling among the optical, electrical and mechanical DOFs, we modulate the output of the LED sinusoidally and vary the modulation frequency. Figure 4a shows the experimental setup for measuring the PVPZ effect. Since the photovoltaic cell is in parallel with the mechanical resonator by construction, the electrical detection of the mechanical actuation must be established differently than that shown in Figs. 2b

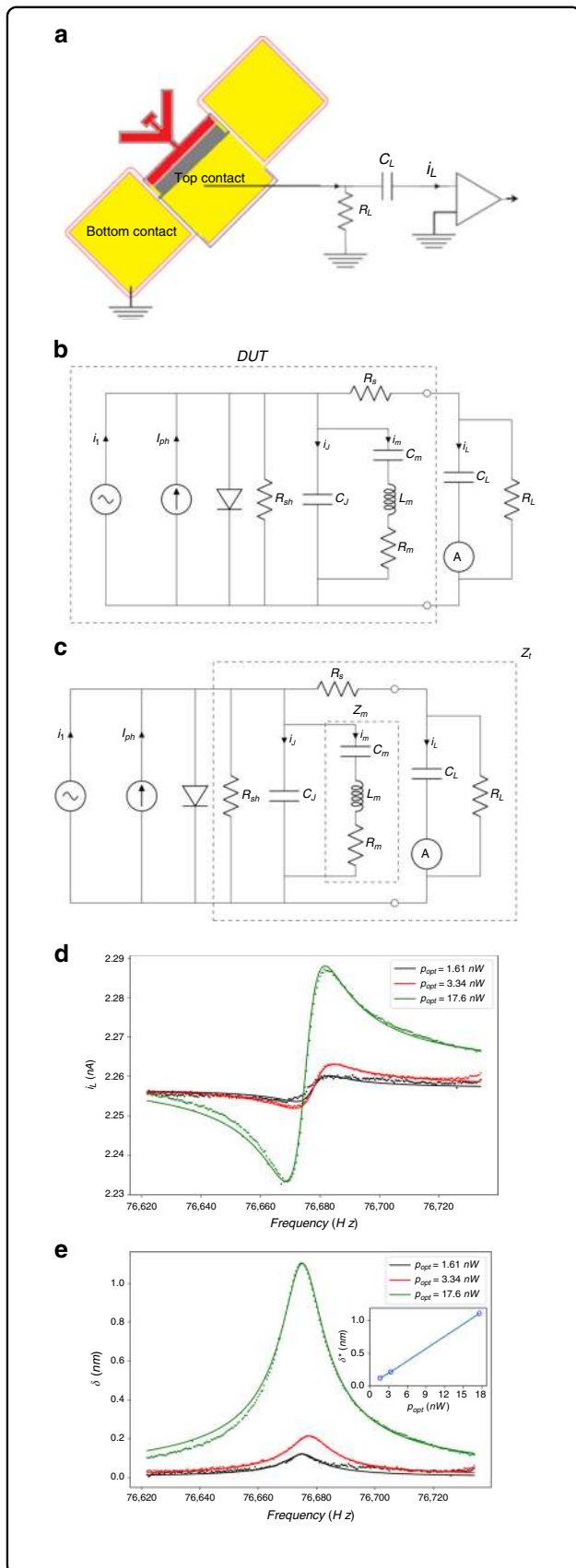


Fig. 4 Optical actuation of the photodiode torsional resonator. a

Experimental setup for measuring the PVPZ effect. The photodiode resonator, optical source, bias T, and preamplifier are placed in a vacuum chamber at a pressure of ~2 mTorr. Similar to the DC measurements, the illuminated section of the resonator is shown in red and illustrates homogeneous illumination. The same 830-nm LED used to characterize the DC efficiency and responsivity is also used here. The bias T is composed of the load capacitance and resistance (C_L and R_L), and i_L is the measured current. **b** PVPZ equivalent circuit. To the left of the diode are the AC and DC photocurrents (i_1 and I_{ph}) photoinduced by the AC and DC optical powers (p_{opt} and P_{opt}) of the LED. To the immediate right of the diode is the BVD circuit similar to Fig. 2b. The load branch is composed of the bias T and is placed at the output terminal or the top electrode of the photodiode. Together, these components establish a DC bias for the PV cell and impedance matching between the device and the measurement circuit. The dashed line encompasses the equivalent circuit of the photovoltaic-piezoelectric resonator or DUT. **c** Same circuit as in Fig. 4b, with the components comprising the total impedance, Z_T , and motional impedance, Z_m , indicated in dashed lines. **d** Frequency response of the measured i_L for P_{opt} of 304 nW and p_{opt} of 1.61, 3.34, and 17.6 nW. The solid lines are fits to the data using Eq. (3) derived from Fig. 4c. Equation (3) depends on 4 parameters [i_1 , C_m , Q , and ω_d] related to the device and the drive/detection parameters. All four parameters are independently determined through the fits, and the parameters are provided in Supplementary Section X. The values are in reasonable agreement with those determined from purely electrical measurements. The measured currents for the p_{opt} values of 1.61 and 3.34 nW have been shifted up so that their background currents align with the background current for $p_{opt} = 17.6$ nW. The fitted Q values are 6875, 5825, and 5625 for p_{opt} values of 1.61, 3.34, and 17.6 nW, respectively. **e** RMS deflection of the tines due to the PVPZ effect the three different optical power levels. The linearity of the maximum deflection with the drive power is shown in the inset as predicted by Eq. (7)

in i_L is maximum when $C_L = C_J$ or when $a = 2$. In our experiments, $C_L = 144$ pF and $C_J = 55$ pF, resulting in $a \sim 3.62$. The device is designed such that R_s is low enough that we can consider it a short circuit and that both R_{sh} and R_L are high enough that they can be considered open circuits for the purpose of AC analysis at frequencies near resonance. To verify the PVPZ effect based on the coupling among the optical, electrical and mechanical DOFs, we drive the resonator optically by modulating the LED at frequencies near the resonant frequency of the device. The measured response (Fig. 4d) agrees well with expectations from the PVPZ circuit (Fig. 4c). The measured resonant frequency is found to be close to the electrically driven case (Fig. 2c), while Q is reduced to ~6100, most likely due to aging of the resonator resulting from lack of sidewall passivation. Similar to the feedthrough current in Fig. 2c, the feedthrough current in Fig. 4d is due to parallel paths through C_L and C_J .

As previously described, it is a good approximation to assume that the motion of the resonator in its torsional mode can be modeled by considering the deflection of the tines as the deflection of cantilevers. In this

approximation, we can determine the complex deflection of the cantilever tips as given by⁴⁵:

$$\delta_z(\omega) = -3\left(\frac{L}{t}\right)^2 \left(\frac{2x_c}{t}\right) d_{23} V_C = -3\left(\frac{L}{t}\right)^2 \left(\frac{2x_c}{t}\right) d_{23} \frac{i_m}{j\omega C_m} \quad (4)$$

where δ_z is the deflection of the tip, x_c is the distance from the center of the beam to the center of the p-n junction (here, $x_c = 752.5$ nm), i_m is the current through the motional arm (R_m , L_m , C_m), L and t are the length and thickness of the tines and V_C is the voltage across C_m . Using analysis of the PVPZ circuit (Fig. 4c), we find that the complex deflection is given by:

$$\delta_z(\omega) = -3\left(\frac{L}{t}\right)^2 \left(\frac{2x_c}{t}\right) d_{23} \frac{i_1 - i_l - i_L}{j\omega C_m} = -3\left(\frac{L}{t}\right)^2 \left(\frac{2x_c}{t}\right) d_{23} \frac{i_1 - i_L \frac{a}{(a-1)}}{j\omega C_m} \quad (5)$$

which can be used to transform the measured i_L to a determination of δ_z (Fig. 4e), based on the fitted values from Supplementary Section X. Figure 4e illustrates a clear resonance (with no antiresonance), as would be expected for a driven simple harmonic oscillator. The peak magnitude is ~ 1.1 nm RMS for an AC optical modulation of only 17.6 nW, corresponding to a non-resonant ($Q = 1$) actuation of $\delta_z \sim 11 \mu\text{m}/\text{W}$.

Starting with Eq. (4) and using $i_m Z_m = i_1 Z_t$, where Z_m is the impedance of the motional arm of Fig. 4c, the expression for the bending of the cantilever is given directly in terms of optical parameters, with no reference to electrical currents, by:

$$|\delta_z(\omega)| = 3\left(\frac{L}{t}\right)^2 \left(\frac{2x_c}{t}\right) d_{23} R_{\text{resp}} p_{\text{opt}} \frac{\omega_0^2 Q}{\omega C_j} \frac{1}{\sqrt{Q^2 \left(\omega_0^2 \frac{C_m}{C_j} + a(\omega_0^2 - \omega^2)\right)^2 + (a\omega\omega_0)^2}} \quad (6)$$

where we have substituted $i_1 = R_{\text{resp}} p_{\text{opt}}$. Since $C_m \ll C_j$ and $Q \gg 1$, the maximum amplitude, or resonant amplitude, is given by:

$$|\delta_z(\omega_{\text{max}})| = 3\left(\frac{L}{t}\right)^2 \left(\frac{2x_c}{t}\right) d_{23} R_{\text{resp}} p_{\text{opt}} Q \frac{1}{\omega_0 C_T} \quad (7)$$

where ω_{max} is the resonant frequency. From Eqs. (6) and (7), we can see clearly that the magnitude of δ_z depends on the product of the optoelectrical material property, R_{resp} , and the piezoelectric constant, d_{23} , and a proportional and linear change in δ_z with p_{opt} is predicted, as shown in the inset of Fig. 4e. We also see that the mechanical motion is described by a conventional

resonant shape without the feedthrough terms present due to electrical detection.

While we have incorporated electrical connections to verify circuit parameters and detect the resonator deflection, this is not required for optical actuation using the PVPZ effect. However, for maximum amplitude, the device needs to be biased at a sufficiently low voltage such that $R_L < V_{\text{oc}}/I_{\text{sc}}$; therefore, a load resistance is still required, which could be incorporated into the device structure. While the load capacitance can be eliminated (i.e., $C_L = 0$, leading to $a = 1$), $\omega_0 R_L C_j > 1$ is still required. By eliminating the contact pad, C_j can be substantially reduced; however, this makes the latter criterion more difficult to achieve. By choosing $R_L \sim 1/(\omega_0 C_j)$ and $I_{\text{sc}} \sim V_{\text{oc}}/R_L$, both criteria are just met, and with full modulation and the p-n junction placed close to the device surface, Eq. (7) simplifies to $|\delta_z(\omega_{\text{max}})| \approx \frac{3}{\sqrt{2}} \left(\frac{L}{t}\right)^2 d_{23} V_{\text{oc}} Q$, which is the maximum amplitude possible via PVPZ optical actuation.

In measurements (not shown), we observe no resonance within our measurement resolution in the vicinity of the fundamental symmetric mode, expected at 26,550 Hz, confirming the nulling of symmetric actuation and detection. We also fabricate control devices with the same geometry but with the tines of the torsional resonator aligned parallel to the [100]- and [010]-directions, which is expected to lead to no PVPZ effect. The results (not shown) indicate no deflection within our measurement resolution, indicating full rejection of the torsional mode and supporting full rejection of symmetric modes in the original geometry.

Historically, the measurement of subtle optically driven forces, such as radiation pressure, has been obscured by the much larger optically induced photothermal forces^{46,47}. While the PVPZ effect is much stronger than radiation pressure effects, the role of photothermal forces must be carefully examined and managed. Our resonator is intentionally designed for use in its fundamental antisymmetric torsional mode to address this concern. The antisymmetric nature of the torsional oscillator design provides actuation and detection of only antisymmetric modes, with symmetric modes leading to cancellation. This cancellation is experimentally confirmed to first order by the two null experiments described above. The illumination wavelength is chosen such that the optical absorption within the GaAs layers is quite axially uniform, reducing photothermal forces. At this wavelength, the optical absorption is still sufficiently high to achieve good photovoltaic efficiency and minimize light transmission through the substrate, reducing another potential source of photothermal drive. Uniform optical illumination and absorption in a photothermal process would only drive symmetric modes since both tines would be actuated in the same way. Therefore, uniform photothermal processes would not actuate the antisymmetric mode or be detected by the antisymmetric piezoelectric detection. However,

nonuniformities in optical actuation could in principle weakly drive the antisymmetric mode photothermally. We estimate the deflection from differential thermal expansion in the z-direction as would be expected from a fully nonuniform photothermal force (i.e., only illuminating a single tine) and find that it is 150 times smaller than the PVPZ effect (Supplementary Section XII) for a single tine. However, due to the nulling from the antisymmetric device design, the observed photothermal actuation would be substantially smaller, indicating that photothermal actuation likely makes a negligible contribution to the observed results. Additionally, the observed currents are in good agreement with expected values based on known and calibrated piezoelectric and photovoltaic effects. We also find (not shown) that the current upon actuation is modified by the bias voltage, which would only be expected for the PVPZ effect⁴⁰.

In conclusion, we have demonstrated the PVPZ effect in a single-crystal GaAs micromechanical torsional resonator photodiode. Observation of this effect in GaAs utilizes its optical, mechanical, piezoelectric and semiconductor properties, coupling them through a device that was intentionally designed to demonstrate the PVPZ effect. The novel torsional resonator design allowed for planar antisymmetric actuation and a high quality factor, exploiting the anisotropic piezoelectric properties of GaAs while minimizing photothermal effects. However, the PVPZ effect could be harnessed in a wide variety of other optomechanical designs, including simple cantilever structures. The device was fabricated using conventional growth and fabrication technology, which allows integration with other device technologies. The PVPZ effect can be utilized for fast, strong optical actuation based on the intrinsic properties of GaAs with known design rules. In addition to this multidomain coupling, the PVPZ effect leads to a larger deflection than competing optical actuation mechanisms. We note that while we have measured the resonator deflection electrically, there is no requirement to have sample leads for the purpose of optical actuation alone. The multidomain coupling between the optical, mechanical and electrical DOFs can be exploited to develop novel devices and capabilities in integrated optoelectromechanical systems. For example, in optical computing, configurable optical circuits can be used to build optical switches⁴⁸ and post-Moore or “More than Moore” technologies such as neuromorphic photonic chips⁴⁹, systems for processing of big data with deep learning⁵⁰ and quantum circuits^{51,52}. With the success of measuring quantized motions of mechanical structures^{53–55}, the PVPZ effect could be another approach to excite phonons and enable bidirectional^{56,57} quantum information transfer between the optical and electrical domains. The PVPZ effect can also be utilized in other III–V piezoelectric device platforms, such as InP and GaN. The

former is of special interest as the prevailing platform for optical communication devices, while the latter platform is now widely used in the manufacture of white light solid-state sources and transistors for high-power electronics.

Materials and methods

Fabrication

A detailed description of the torsional resonator fabrication steps is given in Supplementary Section I. In brief, the torsional resonator geometry is first defined via wet etching, followed by formation of the bottom and top electrical contact pads and then ending with a timed etch release step. There are a total of six process steps consisting of four lithography steps, a back-contact step and a resonator release step. A single chip consists of 326 resonators and is 14 mm × 14 mm. The devices are isolated from each other by wet etching of the heterostructure layers between the devices. The impetus for this step is to minimize stray and feedthrough capacitances and resistances between devices.

Acknowledgements

The heterostructure sample used in this work was MBE grown at McMaster University by Dr. Shahram Tavakoli. We would like to thank Dr. Matthew Minnick, Dr. Martin Gerber and Dr. Kevin Boyd for helpful discussions. A.R. would like to thank Doris Stevanovic for providing training in using the clean room at McMaster University. Natural Sciences and Engineering Research Council of Canada (NSERC) (03736); Canada Foundation for Innovation (CFI) (32168).

Author contributions

A.R. fabricated the devices and performed the measurements. A.R. and R.N.K. conceived and designed the experiment and contributed equally to writing the manuscript.

Conflict of interest

The authors declare no competing interests.

Supplementary information The online version contains supplementary material available at <https://doi.org/10.1038/s41378-021-00249-y>.

Received: 4 September 2020 Revised: 21 January 2021 Accepted: 22 January 2021

Published online: 14 April 2021

References

1. Cripe, J. et al. Measurement of quantum back action in the audio band at room temperature. *Nature* **568**, 364–367 (2019).
2. Sharifi, S. et al. Design of microresonators to minimize thermal noise below the standard quantum limit. *Rev. Sci. Instrum.* **91**, 054504 (2020).
3. Usami, K. et al. Optical cavity cooling of mechanical modes of a semiconductor nanomembrane. *Nat. Phys.* **8**, 168–172 (2012).
4. Okamoto, H. et al. Tunable coupling of mechanical vibration in GaAs microresonators. *Phys. E* **42**, 2849–2852 (2010).
5. Ding, L. et al. High frequency GaAs nano-optomechanical disk resonator. *Phys. Rev. Lett.* **105**, 263903 (2010).
6. Schneider, K. et al. Optomechanics with one-dimensional gallium phosphide photonic crystal cavities. *Optica* **6**, 577–584 (2019).
7. Principe, D., Wiederhecker, G. S., Favero, I. & Frateschi, N. C. Self-sustained laser pulsation in active optomechanical devices. *IEEE Photon. J.* **10**, 1–10 (2018).
8. Gavartin, E. et al. Optomechanical coupling in a two-dimensional photonic crystal defect cavity. *Phys. Rev. Lett.* **106**, 203902 (2011).

9. Ukita, H. A tunable laser diode with a photothermally driven integrated cantilever and related properties. *IEEE J. Sel. Top. Quant. Electron.* **10**, 622–628 (2004).
10. Lagowski, J. & Gatos, H. C. Photomechanical vibration of thin crystals of polar semiconductors. *Surf. Sci.* **45**, 353–370 (1974).
11. Noguchi, A. et al. Single-photon quantum regime of artificial radiation pressure on a surface acoustic wave resonator. *Nat. Commun.* **11**, 1183 (2020).
12. Chenniappan, V. et al. Photostriction actuation of silicon-germanium bilayer cantilevers. *J. Appl. Phys.* **125**, 125106 (2019).
13. Metzger, C. & Karrai, K. Cavity cooling of a microlever. *Nature* **432**, 1002–1005 (2004).
14. Barzanjeh, S. et al. Stationary entangled radiation from micromechanical motion. *Nature* **570**, 480–483 (2019).
15. Boales, J. A., Mateen, F. & Mohanty, P. Micromechanical resonator driven by radiation pressure. *Sci. Rep.* **7**, 16056 (2017).
16. Kundys, B. Photostrictive materials. *Appl. Phys. Rev.* **2**, 011301 (2015).
17. Yu, Y., Nakano, M. & Ikeda, T. Directed bending of a polymer film by light. *Nature* **425**, 145 (2003).
18. Kobatake, S. et al. Rapid and reversible shape changes of molecular crystals on photoirradiation. *Nature* **446**, 778–781 (2007).
19. Brody, P. S. Optomechanical bimorph actuator. *Ferroelectrics* **50**, 27–32 (1983).
20. Shkarin, A. B. et al. Quantum optomechanics in a liquid. *Phys. Rev. Lett.* **122**, 153601 (2019).
21. Figielski, T. Photostriction effect in germanium. *Phys. Status Solidi B* **1**, 306–316 (1961).
22. Eisenbach, C. D. Isomerization of aromatic azo chromophores in poly(ethyl acrylate) networks and photomechanical effect. *Polymer* **21**, 1175–1179 (1980).
23. Brody, P. S. Optomechanical bimorph actuator. *Ferroelectrics* **50**, 27–32 (1983).
24. Seo, Y., Kim, D. & Hall, N. A. Piezoelectric pressure sensors for hypersonic flow measurements. *J. Microelectromech. Syst.* **28**, 271–278 (2019).
25. Kim, N. et al. Piezoelectric pressure sensor based on flexible gallium nitride thin film for harsh-environment and high-temperature applications. *Sens. Actuat. A Phys.* **305**, 111940 (2020).
26. Gesing, A. L. et al. On the design of a MEMS piezoelectric accelerometer coupled to the middle ear as an implantable sensor for hearing devices. *Sci. Rep.* **8**, 3920 (2018).
27. Chen, Z. H. et al. The design of aluminum nitride-based lead-free piezoelectric MEMS accelerometer system. *IEEE Trans. Electron Devices* **67**, 4399–4404 (2020).
28. Chandrashekhar, V. A microchip microcontroller-based transducer controller for non-contact scanning probe microscopy with phaselocked loop, amplitude, and Q control. *Rev. Sci. Instrum.* **91**, 023705 (2020).
29. Castellanos-Gomes, A., Agrait, N. & Rubio-Bollinger, G. Dynamics of quartz tuning fork force sensors used in scanning probe microscopy. *Nanotechnology* **20**, 215502 (2009).
30. An, S. et al. Quartz tuning fork-based frequency modulation atomic force spectroscopy and microscopy with all digital phase-locked loop. *Rev. Sci. Instrum.* **83**, 113705 (2012).
31. Yamada, Y., Ichii, T., Utsunomiya, T. & Sugimura, H. Simultaneous detection of vertical and lateral forces by bimodal AFM utilizing a quartz tuning fork sensor with a long tip. *Jpn. J. Appl. Phys.* **58**, 095003 (2019).
32. Essig, S. et al. Raising the one-sun conversion efficiency of III–V/Si solar cells to 32.8% for two junctions and 35.9% for three junctions. *Nat. Energy* **2**, 17144 (2017).
33. Chen, H. et al. A 19.9%-efficient ultrathin solar cell based on a 205-nm-thick GaAs absorber and a silver nanostructured back mirror. *Nat. Energy* **4**, 761–767 (2019).
34. Bauhuis, G. J. et al. 26.1% thin-film GaAs solar cell using epitaxial lift-off. *Sol. Energy Mater. Sol. Cells* **93**, 1488–1491 (2009).
35. Simon, J. et al. GaAs solar cells grown on intentionally contaminated GaAs substrates. *J. Cryst. Growth* **541**, 125668 (2020).
36. Masmanidis, S. C. et al. Multifunctional nanomechanical systems via tunably coupled piezoelectric actuation. *Science* **317**, 780–783 (2007).
37. Soderkvist, J. & Hjort, K. The piezoelectric effect of GaAs used for resonators and resonant sensors. *J. Micromech. Microeng.* **4**, 28–34 (1994).
38. Knobel, R. G. & Cleland, A. N. Nanometre-scale displacement sensing using a single electron transistor. *Nature* **424**, 291–293 (2003).
39. Okamoto, H. et al. Coherent phonon manipulation in coupled mechanical resonators. *Nat. Phys.* **9**, 480–484 (2013).
40. Rampal, A. *Opto- and Electro-mechanical Coupling Between The Depletion and The Piezoelectric Region of a GaAs Micro Torsional Resonator Photodiode*. PhD thesis (McMaster University, 2017).
41. Hafner, E. The piezoelectric crystal unit – definitions and methods of measurement. *Proc. IEEE* **57**, 179–201 (1969).
42. Borrielli, A. et al. Wideband mechanical response of a high-Q silicon double-paddle oscillator. *J. Micromech. Microeng.* **21**, 065019 (2011).
43. Kleiman, R. N. et al. Single-crystal silicon high-Q torsional oscillators. *Rev. Sci. Instrum.* **56**, 2088–2091 (1985).
44. Nelson, J. *The Physics of Solar Cells* (Imperial College Press, 2003).
45. Soderkvist, J. Similarities between piezoelectric, thermal and other internal means of exciting vibrations. *J. Micromech. Microeng.* **3**, 24–31 (1993).
46. Jones, R. V. & Richards, J. C. S. The pressure of radiation in a refracting medium. *Proc. R. Soc. Lond. A* **221**, 480–498 (1954).
47. Jones, R. V. & Leslie, B. The measurement of optical radiation pressure in dispersive media. *Proc. R. Soc. Lond. A* **360**, 347–363 (1978).
48. Haffner, C. et al. Nano-opto-electro-mechanical switches operated at CMOS-level voltages. *Science* **336**, 860–864 (2019).
49. Tait, A. N., de Lima, T. F. & Zhou, E. Neuromorphic photonic networks using silicon photonic weight banks. *Sci. Rep.* **7**, 7430 (2017).
50. Shen, Y. et al. Deep learning with coherent nanophotonic circuits. *Nat. Photon.* **11**, 441–446 (2017).
51. Wang, J. et al. Multidimensional quantum entanglement with large-scale integrated optics. *Science* **360**, 285–291 (2018).
52. Elshaari, A. W. et al. Hybrid integrated quantum photonic circuits. *Nat. Photon.* **14**, 285–298 (2020).
53. O’Connell, A. D., Hofheinz, M. & Ansmann, M. Quantum ground state and single-phonon control of a mechanical resonator. *Nature* **464**, 697–703 (2010).
54. Chan, J. et al. Laser cooling of a nanomechanical oscillator into its quantum ground state. *Nature* **478**, 89–92 (2011).
55. Teufel, J. D. et al. Sideband cooling of micromechanical motion to the quantum ground state. *Nature* **475**, 359–363 (2011).
56. Vainsencher, A., Satzinger, K. J., Peairs, G. A. & Cleland, A. N. Bi-directional conversion between microwave and optical frequencies in a piezoelectric optomechanical device. *Appl. Phys. Lett.* **91**, 033107 (2016).
57. Wu, M., Zeuthen, E., Balam, K. C. & Srinivasan, K. Microwave-to-optical transduction using a mechanical supermode for coupling piezoelectric and optomechanical resonators. *Phys. Rev. Appl.* **13**, 014027 (2020).